Research Square

Preprints are preliminary reports that have not undergone peer review.
They should not be considered conclusive, used to inform clinical practice,
or referenced by the media as validated information.

Substantial Reduction of Hole Injection Barrier at the Au/Rubrene Organic Semiconductor Interface Using PFBT Self-Assembled Monolayers

Woojin Shin
Kangwon National University
Hyunbok Lee
hyunbok@kangwon.ac.kr

Kangwon National University

Article

Keywords:

Posted Date: November 12th, 2026

DOI: https://doi.org/10.21203/rs.3.rs-11345272/v1

License: This work is licensed under a Creative Commons Attribution 4.0 International License.
Read Full License

Additional Declarations: No competing interests reported.

Substantial Reduction of Hole Injection Barrier at the Au/Rubrene Organic Semiconductor Interface Using PFBT Self-Assembled Monolayers

Woojin Shin and Hyunbok Lee*

Department of Semiconductor Physics and Institute of Forest Science, Kangwon National University, 1 Gangwondaehak-gil, Chuncheon-si, Gangwon-do 24341, Republic of Korea

*Corresponding author: hyunbok@kangwon.ac.kr

Abstract

Surface functionalization using self-assembled monolayers (SAMs) is an effective and widely adopted strategy for optimizing the charge injection and interfacial energetics in organic electronic devices. In particular, 2,3,4,5,6-pentafluorothiophenol (PFBT) SAMs are widely employed to augment the work function of noble metal electrodes, such as Au, and favorably template organic semiconductor molecular packing. However, comprehensive *in situ* spectroscopic investigations detailing the thickness-dependent energy-level alignment across the PFBT-modified Au/organic semiconductor interface remain scarce. This study investigates the interfacial electronic structures of 5,6,11,12-tetraphenylnaphthacene (rubrene) deposited on air-exposed Au (Air-Au), ultraviolet-ozone-treated Au (UVO-Au), and UVO-Au-functionalized PFBT (UVO-Au/PFBT) using *in situ* X-ray and ultraviolet photoelectron spectroscopy (XPS and UPS). High-resolution XPS reveals that UV–O_3 pre-activation forms an ultrathin gold oxide (AuO_x) layer, thereby dramatically enhancing the chemisorption kinetics and packing density of the PFBT SAM. While UV–O_3 treatment alone increases the work function of Au from 4.78 to 5.06 eV, subsequent PFBT chemisorption further elevates it to 5.33 eV via a pronounced permanent dipole moment directed toward the substrate. Consequently, the hole injection barrier at the Au/rubrene interface is progressively reduced from 0.65 eV for Air-Au to 0.40 eV for UVO-Au and ultimately down to 0.27 eV for UVO-Au/PFBT. This dramatic reduction reaches the thermodynamic Fermi-level pinning regime, providing direct spectroscopic evidence for establishing near-Ohmic contacts. These findings offer fundamental insights into contact-resistance minimization and interface design for high-performance organic optoelectronic devices.

Keywords: PFBT, self-assembled monolayer, rubrene, UPS, energy-level alignment, hole injection barrier

Introduction

Organic semiconductors continue to attract intensive research attention for next-generation flexible displays, wearable bioelectronics, and large-area optoelectronics owing to their mechanical flexibility, low-temperature processability, and molecularly tunable electronic structures[1-6]. Nevertheless, realizing the full device potential of organic field-effect transistors (OFETs) is frequently hindered by the interfacial contact resistance at the metal electrode/organic interface[7,8]. In high-mobility organic semiconductors, the overall device performance is often contact-limited, rather than channel-limited. Because the intrinsic charge carrier densities in pristine organic semiconductors are negligible, efficient charge injection from the source/drain contacts directly governs the operating currents, switching speeds, and power dissipation.

Interfacial engineering using self-assembled monolayers (SAMs) is a well-established and highly modular methodology for overcoming high contact resistance[9-12]. Chemisorbed SAMs spontaneously organize into densely packed, thermodynamically stable monomolecular layers on conducting or semiconducting substrates. The constituent molecules can be synthetically engineered to possess tailored permanent dipole moments, thereby establishing an electrostatic potential step that tunes the effective work function of the electrode. Simultaneously, SAM modification tailors the substrate surface energy, providing steric and electronic templates that favorably direct the molecular packing, crystalline domain size, and molecular orientation of the overlying conjugated active layers.

Various anchoring chemistries have been exploited depending on the substrate material and device geometry. On transparent conductive oxides and metal-oxide gate dielectrics, phosphonic acid-based SAMs are preferred because of their robust multidentate condensation bonds[13-17]. On noble metal surfaces, particularly gold (Au), thiol-based molecules such as 2,3,4,5,6-pentafluorothiophenol (PFBT) are typically used for Au surfaces[18-21]. In PFBT, the

terminal thiol (–SH) group undergoes oxidative chemisorption to form robust covalent Au–S bonds. Meanwhile, the highly electronegative fluorine atoms withdraw electrons from the conjugated aromatic ring, producing an intrinsic molecular dipole moment directed along the molecular backbone toward the Au substrate. This dipole vector, combined with the metal–molecule charge rearrangement, substantially enhances the Au work function, thereby promoting hole injection into the p-type organic channels.

Despite the ubiquity of PFBT in organic electronics, fundamental questions regarding the exact thickness-dependent evolution of the frontier orbital energies across PFBT-modified Au/organic interfaces remain unanswered. Separate *ex situ* characterizations of isolated electrodes and organic films often yield scattered energy values that deviate from the intrinsic energy-level alignment because they neglect critical interfacial phenomena such as interface dipoles and band bending. To resolve the intrinsic energetics without experimental artifacts, stepwise molecular deposition and spectroscopic analysis must be performed *in situ* under ultrahigh-vacuum (UHV) conditions. Such depth-resolved photoemission measurements provide unambiguous quantitative access to critical interfacial parameters, including vacuum-level and highest occupied molecular orbital (HOMO)-level shifts and spatial band bending across the interfacial zone[22-25].

This study presents comprehensive *in situ* X-ray and ultraviolet photoelectron spectroscopy (XPS and UPS, respectively) investigations of the thickness-dependent energy-level alignments of 5,6,11,12-tetraphenylnaphthacene (rubrene) deposited on three distinct Au surfaces: air-exposed Au (Air-Au), ultraviolet–ozone (UV–O_3)-treated Au (UVO-Au), and UVO-Au functionalized with a PFBT SAM (UVO-Au/PFBT). Rubrene was chosen as the benchmark p-channel organic semiconductor because of its exceptionally high intrinsic hole mobility and prominent utilization in single-crystal and thin-film OFETs[26]. The study demonstrates that UV–O_3 pre-activation is decisive for forming an activated AuO_x layer, which

facilitates the formation of a dense, well-ordered PFBT monolayer. Most importantly, the resulting work function increase in UVO-Au/PFBT (5.33 eV) dramatically reduces the interfacial hole-injection barrier to 0.27 eV. It is shown that this value corresponds to the onset of Fermi-level pinning, thereby establishing an efficient near-Ohmic contact capable of drastically mitigating the contact resistance in p-type organic electronic devices.

Experimental details

Detailed specifications of the integrated UHV deposition and surface analysis systems have been described in previous studies[27]. A 90 nm-thick Au electrode film (purity: 99.99%, Taewon Scientific Co., South Korea) was deposited via electron-beam evaporation in a high-vacuum chamber onto pre-cleaned indium tin oxide (ITO)-coated glass substrates (AMG, South Korea). To investigate the role of surface activation, the Au substrates were subjected to UV–O_3 treatment for 5 min at room temperature (~300 K) using a PSDP-UV4T cleaner (Novascan Technologies Inc., United States). For SAM formation, the freshly UV–O_3-activated Au substrates were immersed in a 10 mM solution of PFBT (purity: 97%; Sigma-Aldrich Inc., United States) prepared in anhydrous ethanol for 30 min. Following the immersion step, the functionalized substrates were thoroughly rinsed multiple times with clean ethanol to desorb the physisorbed multilayers and dried under a continuous stream of dry N_2 gas.

Bare Au (Air-Au and UVO-Au) and SAM-modified Au (UVO-Au/PFBT) substrates were promptly transferred to an interconnected multi-chamber UHV preparation system. Rubrene (purity: >99%; Luminescence Technology Co., Taiwan) was sublimed in a stepwise manner at a constant evaporation rate of 0.01 nm s^{-1}. After each progressive deposition step, the sample was transferred *in situ* to the analysis chamber without breaking the vacuum to collect XPS and UPS spectra. The film thickness and growth rate were continuously monitored using a quartz

crystal microbalance (QCM) positioned adjacent to the sample stage, with thickness values calibrated using the attenuation of the substrate core-level photoemission intensities. The base pressures of the preparation and analysis chambers were maintained below 2×10^{-8} Torr and 3×10^{-10} Torr, respectively.

Photoemission spectra were acquired using a hemispherical PHOIBOS 150 electron energy analyzer (SPECS GmbH, Germany) equipped with a standard Al K_α X-ray source ($h\nu$ = 1486.7 eV) for XPS and a He I_α discharge lamp ($h\nu$ = 21.22 eV) for UPS. To determine the secondary electron cutoff (SECO), a sample bias of −5 V was applied during UPS acquisition. The instrumental energy resolutions of the XPS and UPS systems were determined to be 1.2 eV and 0.08 eV, evaluated from the full width at half maximum of the Au $4f_{7/2}$ peak and the Fermi-edge broadening of an Ar^+-sputtered clean Au substrate, respectively.

Results and discussion

Figure 1 shows the density functional theory (DFT) calculation results for an isolated PFBT molecule, performed using the Gaussian 09 package with the B3LYP hybrid functional and a 6–31G(d) basis set[28-30]. The fully relaxed molecular geometry, Mulliken atomic charges, and corresponding electrostatic potential map are displayed in Figures 1(a)–(c). Owing to the strong electronegativity of the fluorine atoms, the electron density is pulled toward the outer periphery, creating an electron-rich environment around the fluorinated ring. This yields a calculated dipole moment of 1.29 Debye oriented from the fluorine atoms toward the thiol hydrogen. However, upon chemisorption onto the Au substrate, the thiol group undergoes deprotonation to form a covalent Au–S bond that modifies the net dipole moment. Furthermore, the resulting electrostatic potential step across the interface is governed by the molecular tilt angle relative to the Au surface. Although a quantitative description of the chemisorbed dipole configuration is beyond the scope of this study, the strong permanent dipole character of the

PFBT molecule is clearly evident.

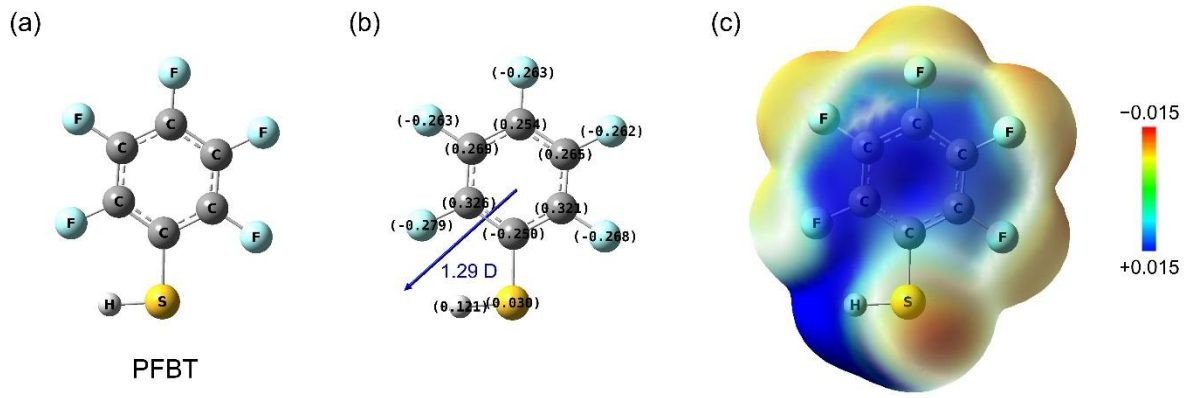


Figure 1. DFT calculations for an isolated PFBT molecule: (a) optimized molecular structure, (b) Mulliken atomic charges with the calculated dipole moment vector, and (c) electrostatic potential map (color scale in atomic units).

The chemisorption characteristics of PFBT on Au electrodes are first examined as a function of UV-O_3 surface pre-treatment. Figures 2(a) and 2(b) show the high-resolution XPS profiles of the F 1s and S 2p core-level regions for the four prepared surfaces: Air-Au, Air-Au/PFBT, UVO-Au, and UVO-Au/PFBT (from top to bottom).

On the Air-Au/PFBT surface, a weak F 1s core-level peak is observed at 687.2 eV, accompanied by a faint S 2p doublet in the 161–164 eV range attributable to covalent Au–S bonding[31]. These low-intensity features indicate that PFBT chemisorption proceeds to a limited extent, resulting in sparse surface coverage. The modest signal-to-noise ratio in the S 2p spectrum is attributed to both the intrinsically low photoionization cross section of sulfur and the low atomic stoichiometry of sulfur within the molecular monolayer. Furthermore, the photoelectron attenuation of the S 2p emission by the overlying upright pentafluorophenyl ring further diminishes its intensity relative to the topmost F 1s core level. In contrast, UV–O_3 pre-treatment produces a reactive, high-surface-energy AuO_x overlayer [Figure 2(a), inset]. This activated interface lowers the kinetic barrier for covalent Au–thiolate coupling, promoting the formation of a dense, well-ordered SAM, as corroborated by the dramatically enhanced F 1s

and S 2p intensities. In the O 1s spectra, the native oxide peak appears at 532.0 eV for Air-Au, whereas the AuO_x component emerges at a significantly lower binding energy of 530.6 eV, highlighting their distinct chemical origins and interfacial roles.

The corresponding UPS spectra depicting the SECO and HOMO regions are shown in Figures 2(c) and 2(d), respectively. The SECO spectra are presented on a kinetic energy scale with the applied sample bias subtracted, allowing direct determination of the substrate work function. Pristine Air-Au exhibited an initial work function of 4.78 eV. This value is substantially lower than that of atomically clean Au (~5.2 eV under UHV), which is a direct consequence of the adsorption of adventitious airborne hydrocarbons[32,33]. These adsorbates induce a push-back effect, compressing metal electron spillover into the bulk and reducing the surface dipole contribution[22]. Immersion of the Air-Au substrate into the PFBT solution moderately increased the work function to 4.88 eV, which was attributed to incomplete PFBT SAM coverage, consistent with the XPS results. This indicates that a well-defined PFBT monolayer does not effectively form on Air-Au, likely because the preexisting adventitious hydrocarbons impede molecular adsorption and close packing. Conversely, UV–O_3 treatment of bare Au (UVO-Au) increases the work function to 5.06 eV owing to the formation of an interface dipole associated with $Au^{\delta+}$–$O^{\delta-}$ bonds[34]. Subsequent functionalization with PFBT (UVO-Au/PFBT) further increased the work function to 5.33 eV. Concurrently, distinct molecular valence features emerge in the 1–9 eV range of the HOMO region, confirming the formation of a well-defined PFBT SAM. This substantial work function enhancement originates from the collective electrostatic potential step generated by the oriented, highly electronegative pentafluorophenyl groups pointing away from the Au substrate.

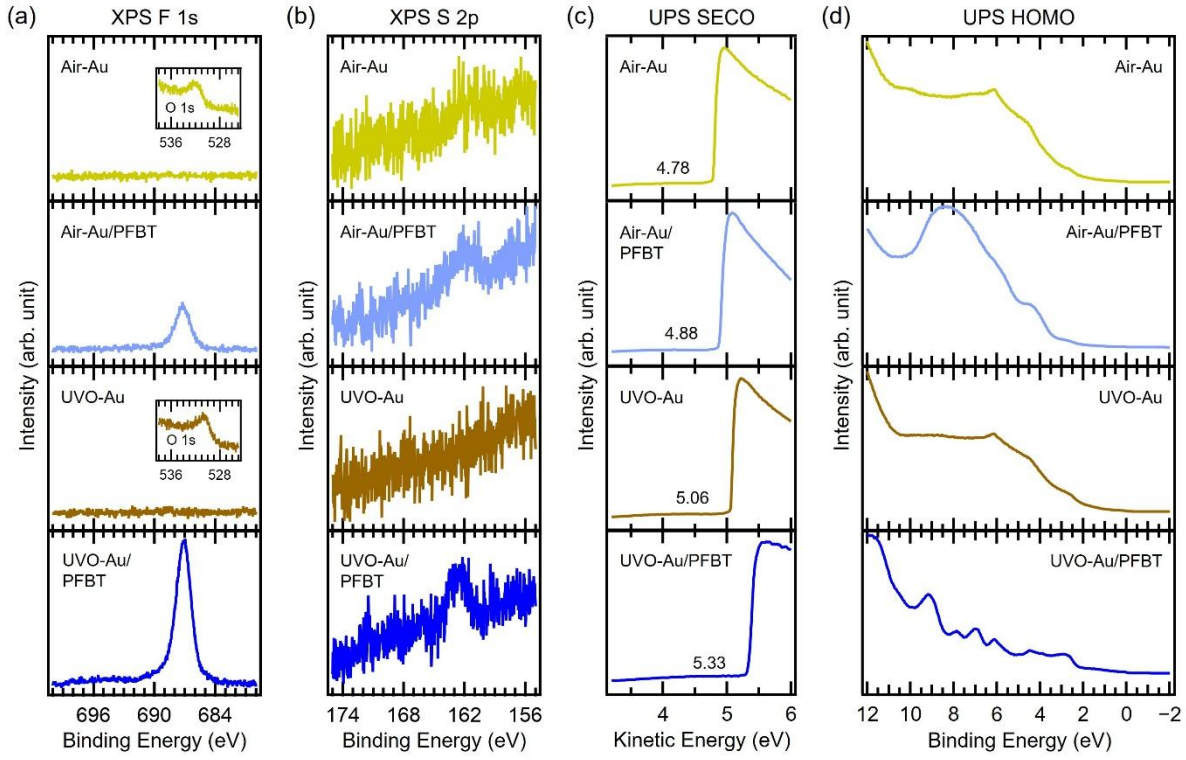


Figure 2. High-resolution XPS core-level spectra of (a) F 1s and (b) S 2p and UPS spectra of the (c) SECO and (d) HOMO regions for Air-Au, Air-Au/PFBT, UVO-Au, and UVO-Au/PFBT surfaces, demonstrating the effect of UV–O_3 pre-treatment on promoting PFBT SAM chemisorption and work function modification. The inset in (a) shows the O 1s core-level spectrum.

To establish the baseline interfacial energetics, rubrene was sequentially evaporated onto the pristine Air-Au substrate. Figures 3(a) and 3(b) show the *in situ* XPS spectra of the Au 4f and C 1s regions across the incremental rubrene deposition stages. The pristine substrate exhibits Au $4f_{7/2}$ and $4f_{5/2}$ spin-orbit doublet peaks at 84.0 and 87.7 eV, respectively. With increasing rubrene overlayer thickness, the Au 4f doublet intensities progressively attenuate without noticeable peak shifts or broadening. The overlayer thickness (d) was calculated using the Beer–Lambert attenuation law as follows:

$$d = \lambda \times \ln\left(\frac{I_0}{I}\right),$$

where I_0 is the pristine substrate intensity, I is the attenuated intensity under rubrene coverage, and λ = 3.7 nm is the inelastic mean free path of Au 4f photoelectrons through rubrene,

calculated from the NIST database[35]. The calibrated thicknesses were determined to be 0.3, 0.7, 1.6, 3.2, 7.4, and 17.4 nm.

As shown in Figure 3(b), the bare Air-Au substrate exhibits an adventitious carbon peak centered at 284.6 eV. Upon rubrene deposition, the C 1s peak rapidly shifts and intensifies, centered at 284.1 eV at 0.3 nm and shifting toward higher binding energy to 284.2 eV at 17.4 nm. Characteristic $\pi \rightarrow \pi^*$ shake-up satellite features emerge above 289.6 eV, confirming the intact π-conjugated electronic structure of rubrene.

The corresponding UPS spectra are shown in Figures 3(c) and 3(d). As shown in the SECO region, the initial work function of Air-Au (4.78 eV) gradually decreases upon rubrene deposition to 4.73, 4.70, 4.68, 4.65, 4.64, and 4.62 eV for thicknesses of 0.3, 0.7, 1.6, 3.2, 7.4, and 17.4 nm, respectively. In the HOMO region, the distinct metallic Fermi edge and Au 5d valence band features vanish as rubrene coverage increases. Characteristic rubrene molecular emission peaks appear at 1.1, 2.7, 3.6, and 4.1 eV. The initial HOMO onset is resolved at 0.65 eV at a coverage of 1.6 nm (a coverage sufficient to establish a contiguous molecular layer). As the film thickens to 17.4 nm, the HOMO onset shifts monotonically toward higher binding energy, arriving at 0.86 eV. This progressive 0.21 eV shift corresponds to downward band bending within the rubrene overlayer, driven by the thermodynamic equilibration of the chemical potentials and charge redistribution across the interface. This trend is consistently observed in the XPS C 1s core-level spectra, albeit with a slight disparity in magnitude arising from the larger probing depth of XPS compared with UPS. Meanwhile, the shift in the HOMO onset (0.21 eV) is comparable to that of the SECO (0.16 eV), indicating a rigid energy-level shift without pronounced interfacial reactions, which may be attributed to adventitious carbon contamination acting as a buffer layer.

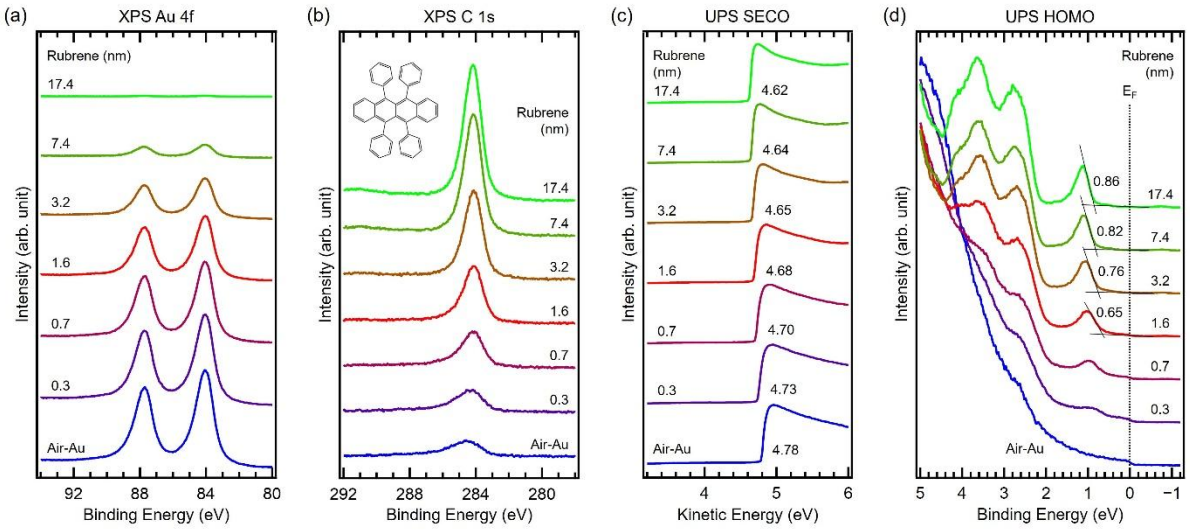


Figure 3. Thickness-dependent *in situ* XPS core-level spectra of the (a) Au 4f and (b) C 1s regions and *in situ* UPS spectra of the (c) SECO and (d) HOMO regions recorded during the sequential deposition of rubrene on the Air-Au substrate. The inset in (b) shows the molecular structure of rubrene. E_F denotes the Fermi level.

Figures 4(a)–(d) show the corresponding *in situ* XPS and UPS spectra of the UVO-Au/rubrene system. The Au 4f core-level spectra [Figure 4(a)] attenuate systematically, yielding calibrated rubrene thicknesses of 0.1, 0.4, 1.3, 2.9, 7.3, and 18.8 nm. Because of the very low surface AuO_x concentration, only an extremely weak feature emerges at higher binding energy, with no other significant changes were detected in the spectra. In the C 1s region [Figure 4(b)], the adventitious carbon peak of the UVO-Au is shifted toward lower binding energy by 0.3 eV relative to that of Air-Au, directly reflecting the increase in the substrate work function. However, its intensity remained comparable to that of Air-Au, which was attributed to the rapid ambient readsorption of adventitious airborne hydrocarbons on the highly reactive, high-surface-energy AuO_x surface during sample loading. Nevertheless, the substantial increase in the work function confirms that the strong interface dipole induced by the underlying AuO_x layer remains robustly preserved despite this unavoidable ambient readsorption. A secondary peak at 287.4 eV signifies oxidized carbon residues formed during the UV–O_3 process. As rubrene evaporated, the dominant rubrene aromatic C 1s component

appears at 284.0 eV and shifted slightly to 284.1 eV at 18.8 nm.

From the UPS SECO region [Figure 4(c)], the work function of pristine UVO-Au was determined to be 5.06 eV. During rubrene growth, the work function decreased monotonically to 4.98, 4.93, 4.89, 4.85, 4.80, and ultimately 4.77 eV at 18.8 nm. In the HOMO region [Figure 4(d)], the rubrene HOMO onset was clearly identified at 0.40 eV at a thickness of 1.3 nm. With increasing film thickness, the onset shifted downward to 0.70 eV at 18.8 nm, representing a downward band bending of 0.30 eV. The hole injection barrier at the immediate interface was thus reduced from 0.65 eV on Air-Au to 0.40 eV on UVO-Au, confirming that elevating the substrate work function directly assisted hole injection. In this case, the SECO and HOMO onset shifts were nearly identical, indicating a rigid band shift resulting from the electronic decoupling of rubrene from the underlying Au substrate by the ultrathin AuO_x interlayer.

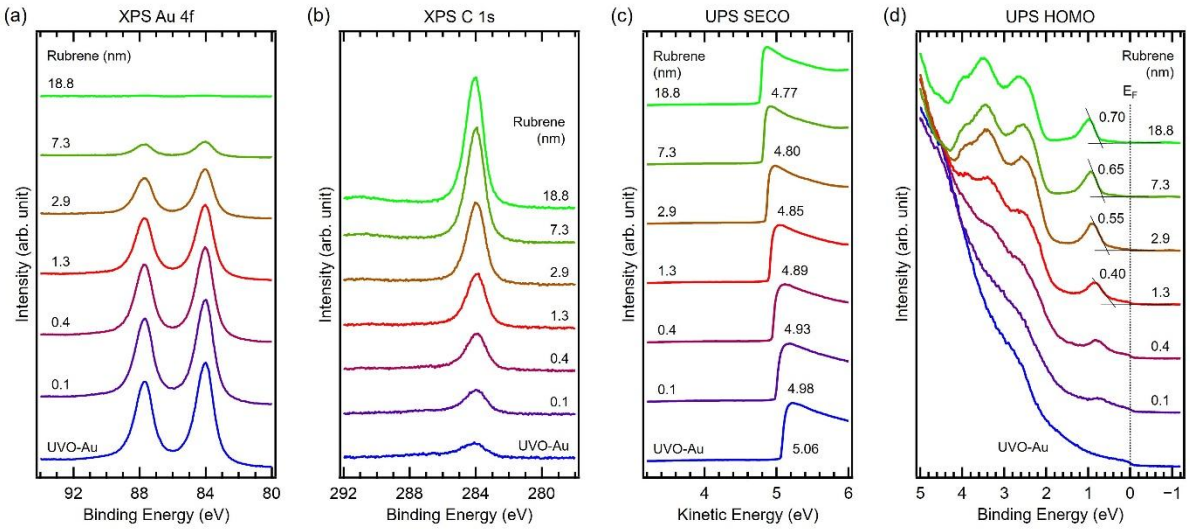


Figure 4. Thickness-dependent *in situ* XPS core-level spectra of the (a) Au 4f and (b) C 1s regions and *in situ* UPS spectra of the (c) SECO and (d) HOMO regions recorded during the sequential deposition of rubrene on the UVO-Au substrate.

The influence of SAM functionalization was investigated by examining the UVO-Au/PFBT/rubrene interface, as shown in Figure 5. As shown in Figure 5(a), the Au 4f doublet attenuated regularly with the rubrene deposition steps corresponding to thicknesses of 0.2, 0.4, 0.9, 2.0, 4.0, and 12.0 nm. In the XPS C 1s spectrum [Figure 5(b)], the substrate shows a distinct

component at 286.8 eV, originating from the fluorinated aromatic carbons (C–F) of the PFBT SAM. As rubrene is deposited, the aromatic C 1s peak at 284.0 eV (0.2 nm) quickly dominates, shifting slightly to 284.1 eV at 12.0 nm.

The UPS SECO spectra in Figure 5(c) reveal a high work function of 5.33 eV for the UVO-Au/PFBT surface. During the initial submonolayer deposition stages (0.2 and 0.4 nm), the work function exhibits an anomalous, transient upward shift to 5.39 and 5.38 eV, respectively. This behavior was absent on both Air-Au and UVO-Au surfaces. This phenomenon is attributed to an interfacial polarization effect induced by ground-state electrostatic coupling between the electron-deficient perfluorinated phenyl rings of the PFBT SAM and the electron-rich, π-conjugated acene core of the adsorbing rubrene molecules. This subtle upward shift can be further rationalized by partial ground-state charge transfer and the cooperative reorientation of interfacial dipole vectors induced by the initial contact of rubrene with the strongly electronegative fluorinated surface. As the rubrene film evolves into the multilayer regime (> 0.9 nm), electrostatic screening effects become dominant, and the work function gradually decreases, saturating at 4.82 eV at 12.0 nm.

In the HOMO region [Figure 5(d)], a weak yet characteristic PFBT HOMO emission is discernible at 1.4 eV on the functionalized substrate. Upon rubrene deposition, the rubrene frontier molecular orbitals develop between the PFBT HOMO and the Fermi level. At a coverage of 0.9 nm, the rubrene HOMO onset is situated at an exceptionally low binding energy of only 0.27 eV. As the rubrene layer thickens to 12.0 nm, this onset shifts progressively to 0.65 eV, revealing a downward band bending of 0.38 eV.

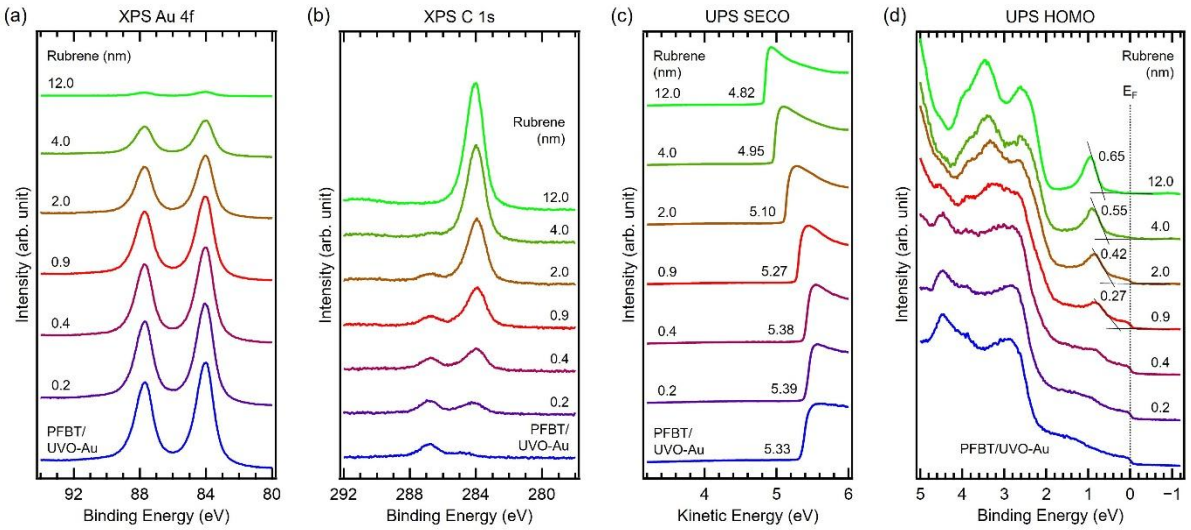


Figure 5. Thickness-dependent *in situ* XPS core-level spectra of the (a) Au 4f and (b) C 1s regions and *in situ* UPS spectra of the (c) SECO and (d) HOMO regions recorded during the sequential deposition of rubrene on the UVO-Au/PFBT substrate.

To synthesize the spectroscopic observations, the complete energy-level diagrams for the three interfaces are illustrated in Figures 6(a)–(c). The lowest unoccupied molecular orbital (LUMO) positions were calculated by adding the transport gap (2.56 eV) of rubrene, obtained from combined UPS and inverse photoelectron spectroscopy literature[36], to the measured HOMO onset energies. Across all three systems, the bulk ionization energy of rubrene converges to 5.47–5.48 eV at the thickest deposition stages, confirming that the bulk intrinsic electronic properties of the organic film remain invariant regardless of the underlying substrate. In the ultrathin regime, minor variations in ionization energy reflect transient polarization effects and potential variations in the initial molecular packing configurations[37,38].

A direct comparison highlights the progressive impact of the interfacial modifications. For Air-Au/rubrene [Figure 6(a)], the low substrate work function (4.78 eV) yields a substantial hole injection barrier of 0.65 eV and an electron injection barrier of 1.91 eV at the interface, followed by a downward band bending of 0.21 eV. This large barrier is a major bottleneck for hole injection. For UVO-Au/rubrene [Figure 6(b)], pre-treating the Au with UV–O_3 elevates the work function to 5.06 eV via the formation of an interface dipole. Consequently, the hole

injection barrier was reduced to 0.40 eV, and the electron injection barrier was increased to 2.16 eV, accompanied by band bending of 0.30 eV. For UVO-Au/PFBT/rubrene [Figure 6(c)], functionalization with the PFBT SAM raised the work function to 5.33 eV, resulting in an ultralow hole injection barrier of only 0.27 eV, an electron injection barrier of 2.29 eV, and band bending of 0.38 eV. However, because these band-bending values were calculated across different final thicknesses, they may vary slightly even at the same thickness.

The energy difference between the UVO-Au/PFBT substrate work function (5.33 eV) and the bulk ionization energy of rubrene (5.47 eV) was only 0.14 eV. According to the integer charge transfer model, when the substrate work function approaches or surpasses the positive integer charge transfer state of an organic semiconductor, spontaneous ground-state charge transfer occurs across the interface[39-41]. This clamps the Fermi level within the organic tail states, a condition known as Fermi-level pinning. Under this condition, the hole injection barrier reaches a fundamental thermodynamic minimum, typically observed to be approximately 0.2–0.3 eV for organic films. Thus, the measured barrier of 0.27 eV for UVO-Au/PFBT/rubrene demonstrates that the interface operates at the threshold of the pinning regime, effectively eliminating injection bottlenecks and forming a near-Ohmic contact for holes.

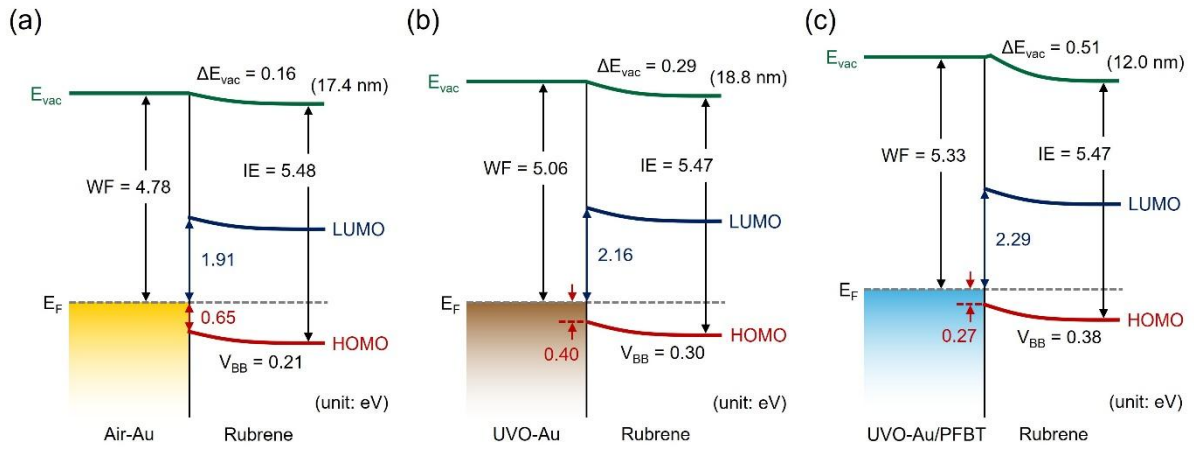


Figure 6. Energy-level diagrams of the (a) Air-Au/rubrene, (b) UVO-Au/rubrene, and (c) UVO-Au/PFBT/rubrene interfaces determined from *in situ* UPS measurements. E_{vac}, *WF*, *IE*,

ΔE_{vac}, and V_{BB} denote the vacuum level, work function, ionization energy, total vacuum-level shift (from the bare substrate to the pristine rubrene bulk), and band bending, respectively. Energy values at the thickest film were independently extracted from SECO and HOMO onsets. All energy values are in units of eV.

Conclusion

In summary, this study elucidated the thickness-dependent interfacial electronic structures and energy-level alignments of rubrene sequentially deposited on Air-Au, UVO-Au, and UVO-Au/PFBT using *in situ* XPS and UPS. UV–O_3 surface pre-treatment was shown to be an indispensable step in forming a reactive AuO_x layer, enabling the formation of a dense, well-ordered PFBT SAM. The strong permanent dipole moment of the chemisorbed PFBT SAM dramatically increased the Au work function to 5.33 eV. Consequently, the hole injection barrier at the Au/rubrene interface was significantly reduced from 0.65 eV on pristine Air-Au to 0.40 eV on UVO-Au, ultimately reaching a minimum of 0.27 eV on the UVO-Au/PFBT electrode. This barrier reduction establishes a Fermi-level-pinned near-Ohmic contact for hole transport. These findings elucidate the physical and chemical mechanisms of SAM-directed contact optimization, offering clear guidelines for minimizing contact resistance in high-performance organic transistors and related optoelectronic devices.

Data availability

The data that support the findings of this study are available from the corresponding author upon reasonable request.

Acknowledgements

The deposition of Au electrodes was performed using an electron-beam evaporation system located at the Department of Semiconductor Physics, Kangwon National University.

Author contributions

W.S. and H.L. wrote the main manuscript text and prepared figures. All authors reviewed the manuscript.

Funding

This study was supported by the National Research Foundation of Korea (RS-2018-NR031068, RS-2025-25405766, and RS-2026-25595532), Korea Institute for Advancement of Technology (KIAT) grant funded by the Korea Government (Ministry of Education) (PP0028088, Semiconductor-Specialized University), and the ANCHOR program through the Gangwon ANCHOR Center funded by the Ministry of Education (MOE) and the Gangwon State (G. S.), Republic of Korea (2026-ANCHOR-10-002).

References

1. Ling, H., Liu, S., Zheng, Z. & Yan, F. Organic flexible electronics. *Small Methods* **2**, 1800070 (2018).

2. Bronstein, H., Nielsen, C. B., Schroeder, B. C. & McCulloch, I. The role of chemical design in the performance of organic semiconductors. *Nat. Rev. Chem.* **4**, 66–77 (2020).

3. Wang, S., Peng, L., Sun, H. & Huang, W. The future of solution processing toward organic semiconductor devices: a substrate and integration perspective. *J. Mater. Chem. C* **10**, 12468–12486 (2022).

4. Ding, L. *et al.* Polymer semiconductors: synthesis, processing, and applications. *Chem. Rev.* **123**, 7421–7497 (2023).

5. Chung, S. *et al.* Structural insights into conjugated polymers for stretchable organic transistors. *Chem. Mater.* **36**, 74–98 (2024).

6. Xu, X., Zhao, Y. & Liu, Y. Wearable electronics based on stretchable organic semiconductors.

Small **19**, 2206309 (2023).

7. Natali, D. & Caironi, M. Charge injection in solution-processed organic field-effect transistors: physics, models and characterization methods. *Adv. Mater.* **24**, 1357–1387 (2012).

8. Waldrip, M., Jurchescu, O. D., Gundlach, D. J. & Bittle, E. G. Contact resistance in organic field-effect transistors: conquering the barrier. *Adv. Funct. Mater.* **30**, 1904576 (2020).

9. Casalini, S., Bortolotti, C. A., Leonardi, F. & Biscarini, F. Self-assembled monolayers in organic electronics. *Chem. Soc. Rev.* **46**, 40–71 (2017).

10. Liu, D. & Miao, Q. Recent progress in interface engineering of organic thin film transistors with self-assembled monolayers. *Mater. Chem. Front.* **2**, 11–21 (2018).

11. Kim, S. Y., Cho, S. J., Byeon, S. E., He, X. & Yoon, H. J. Self-assembled monolayers as interface engineering nanomaterials in perovskite solar cells. *Adv. Energy Mater.* **10**, 2002606 (2020).

12. Li, M., Liu, M., Qi, F., Lin, F. R. & Jen, A. K.-Y. Self-assembled monolayers for interfacial engineering in solution-processed thin-film electronic devices design, fabrication, and applications. *Chem. Rev.* **124**, 2138–2204 (2024).

13. Jang, S. *et al.* Hybrid dielectrics composed of Al_2O_3 and phosphonic acid self-assembled monolayers for performance improvement in low voltage organic field effect transistors. *Nano Converg.* **5**, 20 (2018).

14. Acharya, R., Peng, B., Chan, P. K. L., Schmitz, G. & Klauk, H. Achieving ultralow turn-on voltages in organic thin-film transistors investigating fluoroalkylphosphonic acid self-assembled monolayer hybrid dielectrics. *ACS Appl. Mater. Interfaces* **11**, 27104–27111 (2019).

15. Lin, Y. *et al.* Self-assembled monolayer enables hole transport layer-free organic solar cells with 18% efficiency and improved operational stability. *ACS Energy Lett.* **5**, 2935–2944 (2020).

16. Truong, N. A. *et al.* Tripodal triazatruxene derivative as a face-on oriented hole-collecting monolayer for efficient and stable inverted perovskite solar cells. *J. Am. Chem. Soc.* **145**, 7528–

7539 (2023).

17. Zhang, L. *et al.* Configurational isomerization-induced orientation switching: non-fused ring dipodal phosphonic acids as hole-extraction layers for efficient organic solar cells. *Angew. Chem. Int. Ed.* **63**, e20248960 (2024).

18. Lee, H. *et al.* Rubicene: a molecular fragment of C_{70} for use in organic field-effect transistors. *J. Mater. Chem. C* **2**, 3361–3366 (2014).

19. Fenwick, O. *et al.* Modulating the charge injection in organic field-effect transistors: fluorinated oligophenyl self-assembled monolayers for high work function electrodes. *J. Mater. Chem. C* **3**, 3007–3015 (2015).

20. Yang, M.-Y., Wan, Z.-C., Yu, L.-Q., Cui, W. & Yang, Z.-Y. The factors dominating the effect of electrode modification layer on the work function of the electrode and performances of field-effect transistors. *Chem. Mater.* **38**, 9577–9589 (2026).

21. Rockson, T. K. *et al.* Engineering asymmetric charge injection/extraction to optimize organic transistor performances. *ACS Appl. Mater. Interfaces* **11**, 10108–10117 (2019).

22. Ishii, H., Sugiyama, K., Ito, E. & Seki, K. Energy level alignment and interfacial electronic structures at organic/metal and organic/organic interfaces. *Adv. Mater.* **11**, 605–625 (1999).

23. Koch, N. Organic electronic devices and their functional interfaces. *ChemPhysChem* **8**, 1438–1455 (2007).

24. Lee, H., Cho, S. W. & Yi, Y. Interfacial electronic structure for high performance organic devices. *Curr. Appl. Phys.* **16**, 1533–1549 (2016).

25. Fahlman, M. *et al.* Interfaces in organic electronics. *Nat. Rev. Mater.* **4**, 627–650 (2019).

26. Liu, S., Wu, H., Zhang, X. & Hu, W. Research progress of rubrene as an excellent multifunctional organic semiconductor. *Front. Phys.* **16**, 13304 (2021).

27. Yoo, J. *et al.* Energy level alignment at C_{60}/DTDCTB/PEDOT:PSS interfaces in organic photovoltaics. *Appl. Surf. Sci.* **402**, 41–46 (2017).

28. Gaussian 09 v. E.01 (Gaussian Inc. , Wallingford CT, 2009).

29. Becke, A. D. Density-functional thermochemistry. III. The role of exact exchange. *J. Chem. Phys.* **98**, 5648–5652 (1993).

30. Lee, C., Yang, W. & Parr, R. G. Developmenet of the Colle-Salvetti correlation-energy formula into a functional of the electron density. *Phys. Rev. B* **37**, 785–789 (1988).

31. Castner, D. G., Hinds, K. & Grainger, D. W. X-ray photoelectron spectroscopy sulfur 2p study of organic thiol and disulfide binding interactions with gold surfaces. *Langmuir* **12**, 5083–5086 (1996).

32. Turetta, N., Sedona, F., Liscio, A., Sambi, M. & Samori, P. Au(111) surface contamination in ambient conditions: unravelling the dynamics of the work function in air. *Adv. Mater. Interfaces* **8**, 2100068 (2021).

33. Choi, S. *et al.* Influence of storage conditions on the electronic structure of Au and interfacial state formation with C_{60}. *Appl. Surf. Sci.* **684**, 161960 (2025).

34. Rentenberger, S., Vollmer, A., Zojer, E., Schennach, R. & Koch, N. UV/ozone treated Au for air-stable, low hole injection barrier electrodes in organic electronics. *J. Appl. Phys.* **100**, 053701 (2006).

35. Powell, C. J. & Jablonski, A. *NIST electron effective-attenuation-length database - Version 1.3*. (National Institute of Standards and Technology, 2011).

36. Jung, K. *et al.* Elucidation of hole transport mechanism in efficient energy cascade organic photovoltaics using triple donor system. *Appl. Surf. Sci.* **576**, 151747 (2022).

37. Amy, F., Chan, C. & Kahn, A. Polarization at the gold/pentacene interface. *Org. Electron.* **6**, 85–91 (2005).

38. Chen, W. *et al.* Molecular orientation-dependent ionization potential of organic thin films. *Chem. Mater.* **20**, 7017–7021 (2008).

39. Braun, S., Salaneck, W. R. & Fahlman, M. Energy-level alignment at organic/metal and

organic/organic interfaces. *Adv. Mater.* **21**, 1450–1472 (2009).

40. Yang, J.-P. *et al.* Fermi-level pinning appears upon weak electrode-organic contact without gap states: A universal phenomenon. *Org. Electron.* **48**, 172–178 (2017).

41. Lee, H., Jeong, J., Yi, Y. & Lee, H. Electronic structure and Fermi-level pinning of indigo for application in environment-friendly devices. *Appl. Surf. Sci.* **484**, 808–813 (2019).